Supporting Information

Wafer-Scale and Wrinkle-free Epitaxial Growth of Single-Orientated Multi-layer Hexagonal Boron Nitride on Sapphire

A-Rang Jang[†, ‡, ⊥], *Seokmo Hong*[†], *Chohee Hyun*[‡], *Seong In Yoon*[‡], *Gwangwoo Kim*[‡], *Hu Young Jeong*[§], *Tae Joo Shin*[§], *Sung O Park*[∥], *Kester Wong*[∥], *Sang Kyu Kwak*[¶, ∥], *Noejung Park*[¶, #], *Kwangnam Yu*[∇], *Eunjip Choi*[∇], *Artem Mishchenko*[□], *Freddie Withers*[□], *Kostya S. Novoselov*[□], *Hyunseob Lim*[†, ⊥, ¶, *], *and Hyeon Suk Shin*[†, ‡, ⊥, ¶, *]

[†]Department of Chemistry, Ulsan National Institute of Science and Technology (UNIST), UNIST-gil 50, Ulsan 44919, Republic of Korea

[‡]Department of Energy Engineering, Ulsan National Institute of Science and Technology (UNIST), UNIST-gil 50, Ulsan 44919, Republic of Korea

[⊥]Low Dimensional Carbon Materials, Ulsan National Institute of Science and Technology (UNIST), UNIST-gil 50, Ulsan 44919, Republic of Korea

[¶]Center for Multidimensional Carbon Materials, Institute of Basic Science, Ulsan 44919, Republic of Korea

[§]UNIST Central Research Facilities (UCRF), Ulsan National Institute of Science and Technology (UNIST), UNIST-gil 50, Ulsan 44919, Republic of Korea

[#]Department of Physics, Ulsan National Institute of Science and Technology (UNIST), UNIST-gil 50, Ulsan 44919, Republic of Korea

[∥] School of Energy and Chemical Engineering, Ulsan National Institute of Science and Technology (UNIST), UNIST-gil 50, Ulsan 44919, Republic of Korea

[∇]Department of Physics, University of Seoul, Seoul 02504, Republic of Korea

[□]School of Physics and Astronomy, University of Manchester, Manchester M13 9PL, UK

*Email: shin@unist.ac.kr (HSS) and hslim@ibs.re.kr (HL)

EXPERIMENTAL METHODS

Growth of multi-layer h-BN on sapphire substrate using LPCVD. h-BN was prepared by a LPCVD method. A sapphire substrate (c-plane) was placed in the middle of a 2-inch alumina tube CVD system, and ammonia borane (97% purity, Sigma-Aldrich) was placed in a sub-chamber. The furnace was heated to 1400 °C under flow of Ar gas (10 sccm) and H_2 gas (10 sccm). The temperature, 1400 ^{o}C, was measured at the surface of the alumina tube where the thermocouple (TC 1) was placed. Separately, we measured the temperature inside a tube by inserting another thermocouple (TC 2) into the tube to compare with the temperature measured by TC1. The temperature difference between TC 1 and TC 2 was less than 10 ^{o}C. Therefore, we believe that the substrate temperature or the gas temperature would not be much different from the reaction temperature (by TC 1) that we described. The sub-chamber was heated to 130 °C for the decomposition of ammonia borane. The growth of multi-layer h-BN on sapphire substrate was initiated by opening a valve of the sub-chamber. After opening a valve of the sub-chamber, we supply the source during 30 min. During the growth, the pressure was maintained at 0.1 Torr. After growth completion, the furnace was cooled down to room temperature under Ar and H_2 gas.

Characterization of *EM*-h-BN. The surface morphology of *EM*-h-BN was characterized by atomic force microscopy (Dimension Icon, Bruker). Raman spectra were measured using a micro Raman spectrometer (alpha300, WITec GmbH) with a 532-nm laser. FTIR spectroscopy was performed on *EM*-h-BN, transferred EM-h-BN, and mechanically exfoliated h-BN in order to compare the quality of h-BN. *EM*-h-BN was transferred and h-BN was mechanically exfoliated onto lightly doped Si/SiO_2 substrates, which are transparent to IR.[1] The UV-visible absorption spectrum (Cary 5000 UV-vis-NIR, Agilent) was measured to estimate the optical band gap of *EM*-h-BN on the sapphire substrate. The optical band gap

energy was determined by using the formula of a direct band gap semiconductor: $\alpha = C(E - E_g)^{1/2}/E$ (where α is the absorption coefficient, C is a constant, E is the photon energy, and E_g is the optical bandgap energy). The plot of $(\alpha E)^2$ vs. E should be a straight line. Therefore, when $(\alpha E)^2 = 0$, E should be equal to E_g. X-ray photoelectron spectra (K-Alpha, Thermo Fisher) were measured to identify the B and N atoms of h-BN. Low voltage Cs aberration-corrected transmission electron microscopy (Titan Cube G2 60-300, FEI), operated at 80 kV with a monochromated electron beam, was used for ultra-high-resolution imaging of h-BN, along with selected area electron diffraction (SAED) and electron energy loss spectroscopy (EELS). *EM*-h-BN was loaded onto an ultra-high vacuum system (~10^{-10} torr) in order to obtain low-energy electron diffraction (SPECTRALEED, Omicron NanoTechnology GmbH) patterns.

Device fabrication and measurement. The synthesized *EM*-h-BN was transferred onto 300 nm SiO_2/Si substrate using Al-etchant. We measured the breakdown voltage of our transferred *EM*-h-BN. The device size was $1\mu m \times 1\mu m$ and the thickness of transferred *EM*-h-BN is about 1.3 nm. Figure R3a shows the tunneling current of transferred *EM*-h-BN is measured and the current level is similar with previous work.[2] The breakdown electric field of 7.8 – 9.2 MV/cm, as shown in Figure R3b. The CVD-grown polycrystalline graphene was transferred on the top of transferred *EM*-h-BN. The electrode pad for graphene FET was patterned through electron beam lithography process (NB3, NANOMEAM LTD), followed by the sequential deposition of titanium (5 nm) and gold (60 nm) using E-beam evaporator (FC-2000, Temescal). Graphene channels were patterned by electron beam lithography and etched by oxygen plasma. The electrical properties of fabricated graphene FETs were measured using vacuum probe station (CRX-4K, Lakeshore) with semiconductor characterization system (4200-SCS, Keithley).

Micro mechanically exfoliated graphene (MME-graphene) encapsulated between *EM*-h-BN and micro mechanically exfoliated hexagonal boron nitride (MME-h-BN) was produced in the following steps and can be seen schematically in Figure S9. Firstly, a MME-h-BN crystal was prepared on a PMMA membrane and used to lift a MME-graphene flake from a SiO_2 substrate using the van der Waals (vdW) forces between neighboring crystals. The MME-h-BN / MME-graphene stack was then brought into contact with the Al_2O_3 / *EM*-hBN substrate encapsulating the MME-graphene between *EM*-h-BN and MME-h-BN. Top gate electrodes were firstly patterned using electron beam lithography followed by evaporation of 5nm Cr / 50 nm Au. This is followed by a second round of E-beam lithography to pattern the hall bar structure formed by the evaporation of 20 nm of Al to create the etch mask, Figure S9(b). A deep etch procedure in freon plasma was then performed to etch away MME-hBN, leaving a hall bar structure[3]. The Aluminum etch mask was washed away in MF319 developer and 1D Electrical contacts[4] were then attached to the graphene electrodes (5 nm Cr / 50 nm Au).

Characterization of graphene on SiO_2 and h-BN substrate. The adsorption peak at 200 nm of the h-BN film corresponds to its optical band gap, and the peak around 270 nm of graphene originates from the π plasmon peak. These results show that h-BN remains after the graphene transfer. The G and 2D peaks of suspended mechanical exfoliated graphene are located at 1581 and 2674 cm^{-1}, respectively. [5] In this experiment, the G and 2D peaks of graphene on SiO_2/Si substrate appear at 1586 and 2677 cm^{-1}, while those of graphene on *EM*-h-BN at 1580 and 2668 cm^{-1}, respectively. The peak positions for graphene on *EM*-h-BN are close to those for suspended graphene, indicating that *EM*-h-BN considerably suppresses the doping of graphene.

MODELING AND SIMULATION DETAILS

Model Structures and Computational Methods. Classical molecular dynamics (MD), molecular mechanics (MM), and density functional theory (DFT) methods were used to investigate the interplay between binding energy and dynamic orientation of h-BN monolayer on the α-Al_2O_3(0001) surface of the film model (i.e. thickness of 2.415 nm), in terms of rotational motion along the surface plane. Al-terminated Al_2O_3(0001) surface model was employed due to the relative surface stability, which was previously reported to be more stable than the O-terminated Al_2O_3(0001) surface [6]. For our *ab-initio* calculations, a vacuum slab of at least 20 Å was introduced along the perpendicular direction of the Al_2O_3(0001) surface plane, where all structures were optimized using the generalized gradient approximation (GGA) method as implemented in the Dmol^3 program [7, 8]. A double numerical polarized (DNP4.4) basis set was used with the Perdew-Burke-Ernzerhof (PBE) exchange-correlation functional [9]. For the Brillouin zone integration, *k*-point mesh sizes of 3×3×2, 3×3×2 and 15×15×1 were used for the bulk α-Al_2O_3, Al_2O_3(0001) surface and single layer h-BN, respectively. Dispersion correction accounting for the van der Waals interaction was implemented based on Grimme's DFT-D2 method [10]. A self-consistent field (SCF) convergence criteria was set to $<1.0\times10^{-6}$ Ha. We used Mulliken charge to describe the electrostatic interaction between h-BN and Al_2O_3(0001), as shown by the calculated partial charges of the geometrically optimized structures; +0.616 *e* for boron and –0.616 *e* for nitrogen in h-BN, and +1.957 *e* for aluminum and –1.305 *e* for oxygen in bulk α-Al_2O_3. For α-Al_2O_3(0001), variable charges were assigned for each surface layer Al (+1.686*e*~+1.980*e*) and O (–1.310*e*~–1.200*e*) atoms. As partial charges were assigned to the (8×8×4) bulk α-Al_2O_3 and (16×16×1) single layer h-BN with 100 Å vacuum slab, the superstructures were then optimized by NPT-MD (i.e. isothermal-isobaric) method using the forcefields extracted from Zhao *et al.* [11] and Saha *et al.* [12] for Al_2O_3 [11] and h-BN [12], respectively. The lattice

parameters for the unit cells were found to be 4.714×4.714×12.768 $Å^3$ for bulk α-Al_2O_3(0001), and 2.450×2.450 $Å^2$ for h-BN. These parameters are in good agreement with previously reported values [13, 14]. MD simulation was run at 1 atm and 300 K for 50ps with the time step of 1fs. The results were collected from the last 20 ps run. To optimize h-BN/Al_2O_3structures, MM simulation was implemented with fitted forcefields [11, 12] and our calculated partial charges. The tolerance of energy, force, and displacement convergence were set to <2.0×10^{-5} kcal/mol, <0.001kcal/mol/Å, and <1.0×10^{-5}Å, respectively. Additionally, we confirmed no bond formation between h-BN and α-Al_2O_3(0001) by the density of states (DOS) analysis. For each geometrically optimized Moiré pattern, the binding energy between the h-BN and the Al_2O_3(0001) surface was calculated as follows:

$$\Delta E_{binding} = E_{total} - E_{h-BN} - E_{substrate}$$

where E_{total} is the total energy of the optimized h-BN/Al_2O_3(0001), $E_{h\text{-}BN}$ is the energy of h-BN in vacuum, and $E_{substrate}$ is the energy of Al_2O_3(0001) substrate.

Moiré Pattern calculation. Moiré pattern was defined for specific h-BN rotation angle (θ), which is derived by pair indies (n, m) in the following equation [15, 16]:

$$\cos(\theta) = \frac{n^2 + 4nm + m^2}{2(n^2 + nm + m^2)}$$

We used two base unit cells, $R30°$ and $R90°$, as shown in Figure S8 to model the rotational-dependency of binding energy within 0 – 120^o because the restricted orientation angle range for each base unit cell vector is 0 – 60^o [10, 11]. The first unit cell model corresponds to (9×9) h-BN with 30^o rotation on $(\frac{8}{3}\sqrt{3} \times \frac{8}{3}\sqrt{3})$ Al_2O_3 (0001), which was observed experimentally. The other model corresponds to the h-BN at 90^o rotation that shares the same superstructure and geometry with the former system. Note that the $30^o \leq \theta < 90^o$ systems are constructed

based on the first (*R*30°) model, whereas the $90^o \leq \theta \leq 120^o$ and $0^o \leq \theta < 30^o$ systems are based on the second (*R*90°) model. The cell parameters for both sets of models corresponding to each rotation angle are provided in Table S1.

Simulation Results. Binding energies of h-BN/Al_2O_3(0001) were described by non-bonding interaction composed of van der Waals (vdW) and electrostatic (*ES*) interaction energies. We calculated the binding energy per boron-nitrogen atom pair at different rotational angles along the surface plane. At *R*30° and *R*90° rotational angles, h-BN adsorbed on Al_2O_3(0001) more strongly than at other orientation angles; adsorption was the strongest at *R*30° as shown in Fig. 3d. The binding energy was predominantly influenced by the *ES* interaction rather than the vdW interaction. *ES* interaction contributions indicated that the *R*30° and *R*90° models were more stable than h-BN/Al_2O_3(0001) at other rotation angles. However, we note that the vdW interaction in the *R*90° system was weaker than in the *R*30° system because of the close proximity of h-BN on Al_2O_3(0001). In Figure S8, these two structures are easily distinguishable by the h-BN atom positions located at 0.304 nm above the α-Al_2O_3(0001) surface, where nitrogen atoms are located on top of the Al-terminated layer for *R*30°, and boron atoms are on top of the surface O-layer for *R90°*. The shortest interface distance between h-BN and Al_2O_3(0001) for *R*30° and *R*90° are 2.978 and 3.031Å, respectively. This means that the atomic configurations of relatively adjacent h-BN to the surface at *R*90° are less favourable than those in the *R*30° system because of the repulsive vdW interactions between boron and oxygen atoms. By contrast, 30° rotated h-BN was the most strongly attracted to Al_2O_3(0001) surface by strong vdW and *ES* interactions.

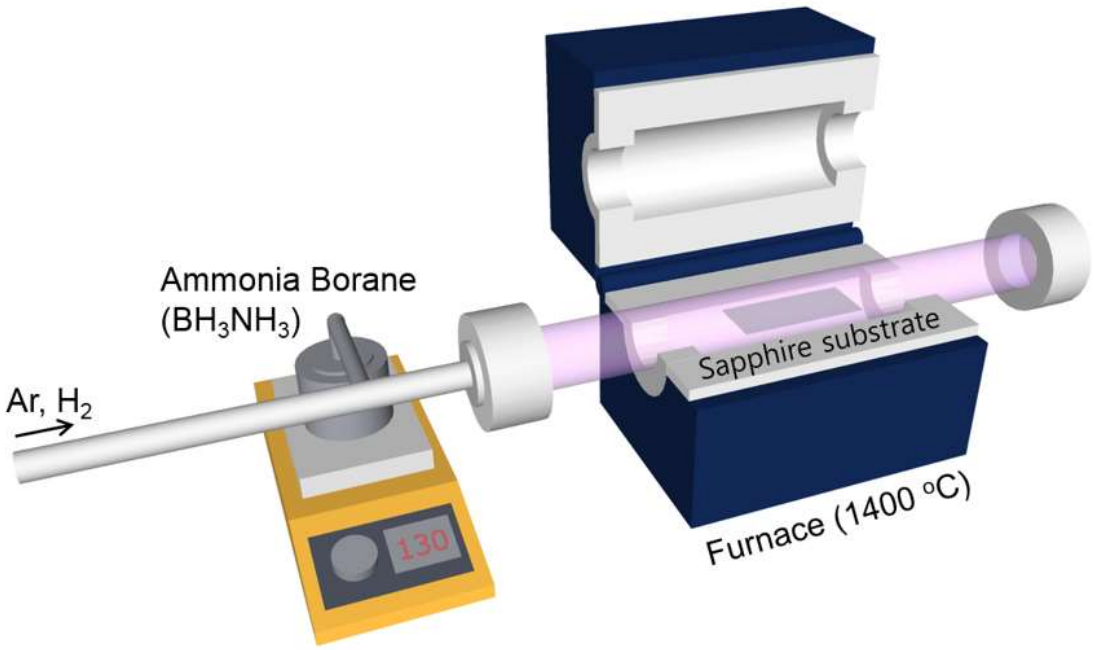

Figure S1. Schematic of the LPCVD system used for multi-layer h-BN growth on sapphire substrate.

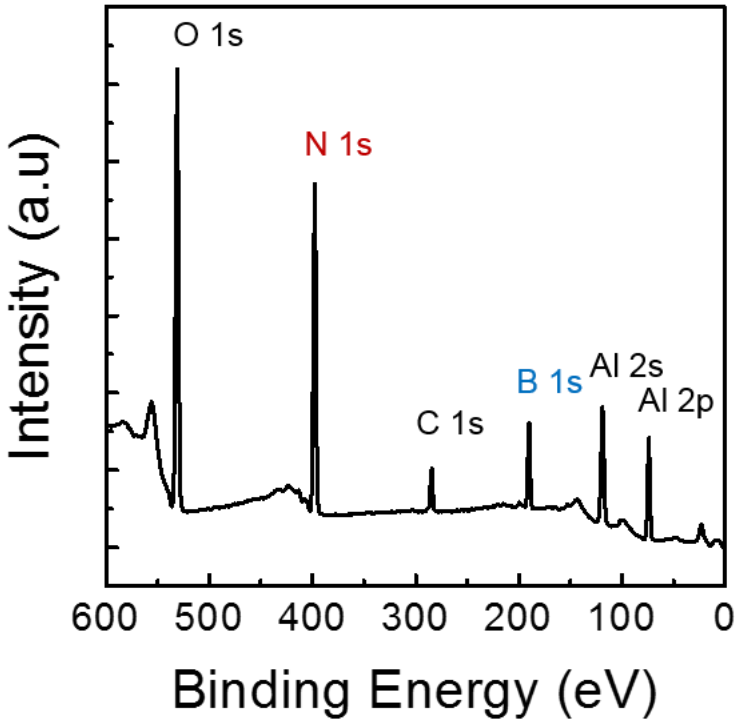

Figure S2. XPS survey spectra of *EM*-h-BN on sapphire substrate.

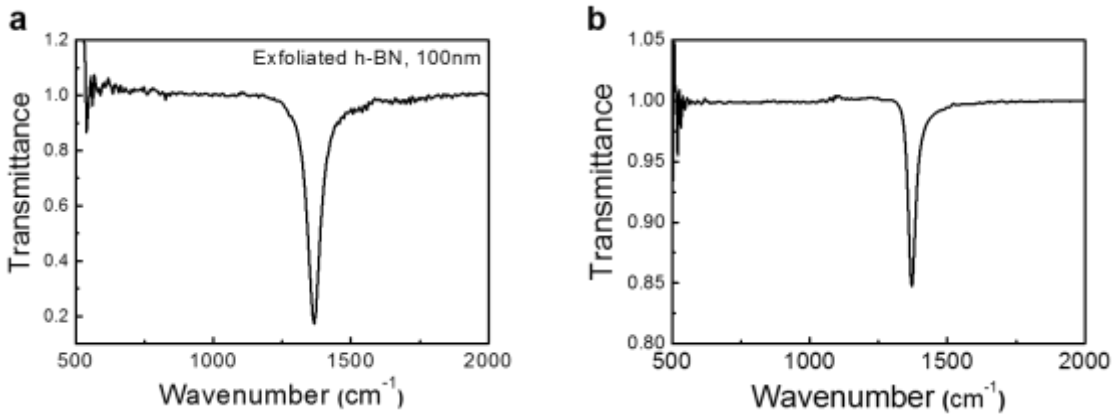

Figure S3. FTIR spectra of (**a**) mechanically exfoliated h-BN and (**b**) transferred *EM*-h-BN on SiO_2/Si substrate.

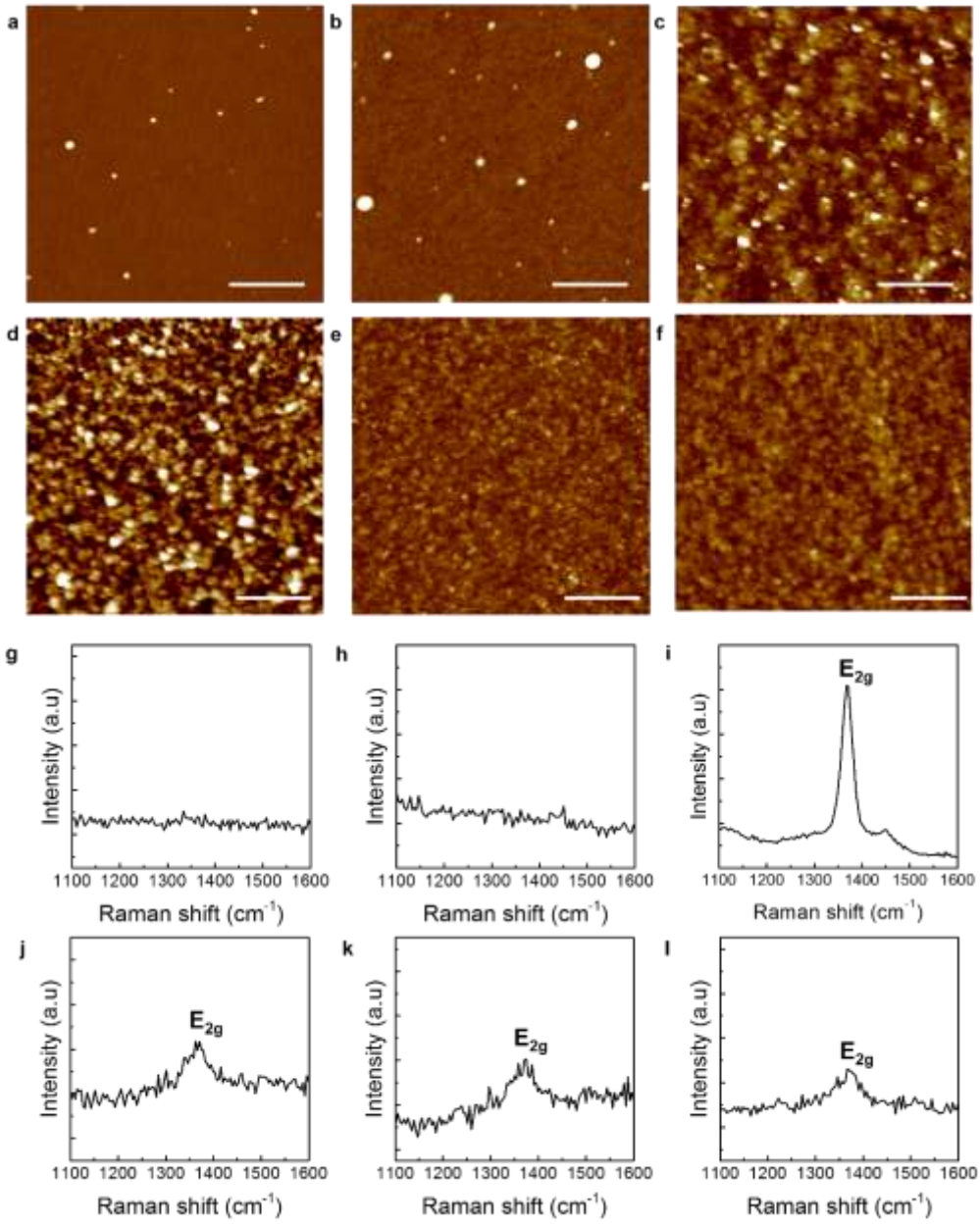

Figure S4. AFM images of **(a)** bare sapphire and **(b)** SiO_2/Si substrates. AFM images of h-BN grown on SiO_2/Si substrate at **(c)** 1100 °C, and h-BN grown on sapphire substrate at **(d)** 1100 °C, **(e)** 1200 °C, and **(f)** 1300 °C. Scale bar is 500 nm. Raman results of **(g)** bare sapphire and **(h)** SiO_2/Si substrate. Raman results of h-BN grown on SiO_2/Si substrate at **(i)** 1100 °C, and h-BN grown on sapphire substrate at **(j)** 1100 °C, **(k)** 1200 °C, and **(l)** 1300 °C.

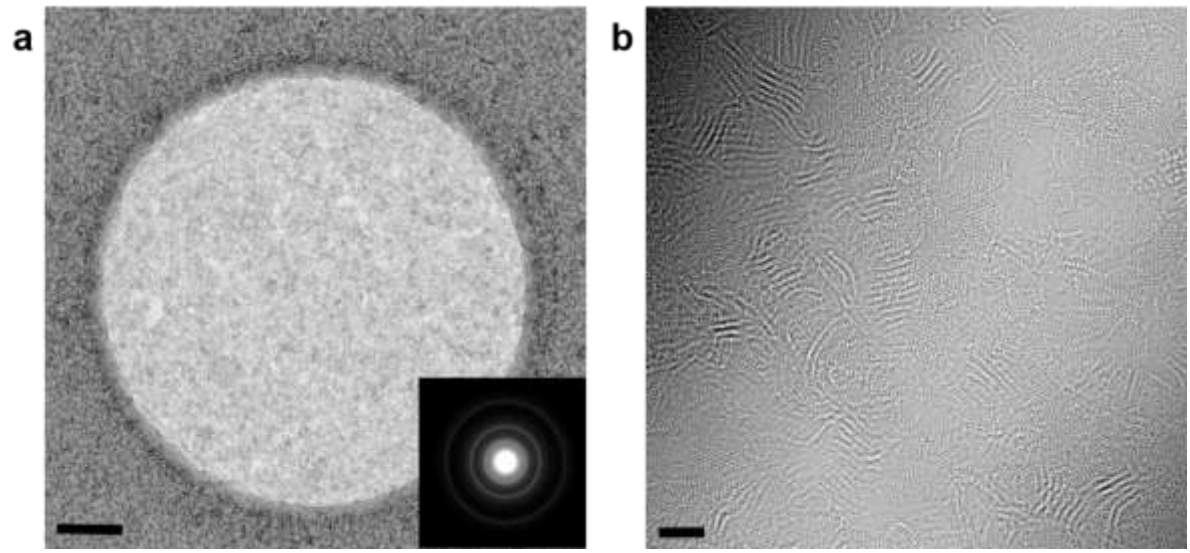

Figure S5. (**a**) Low-magnification (scale bar is 200 nm), diffraction pattern (insert), and (**b**) high-magnification TEM image of small h-BN particles grown on SiO_2/Si substrate. (scale bar is 2 nm)

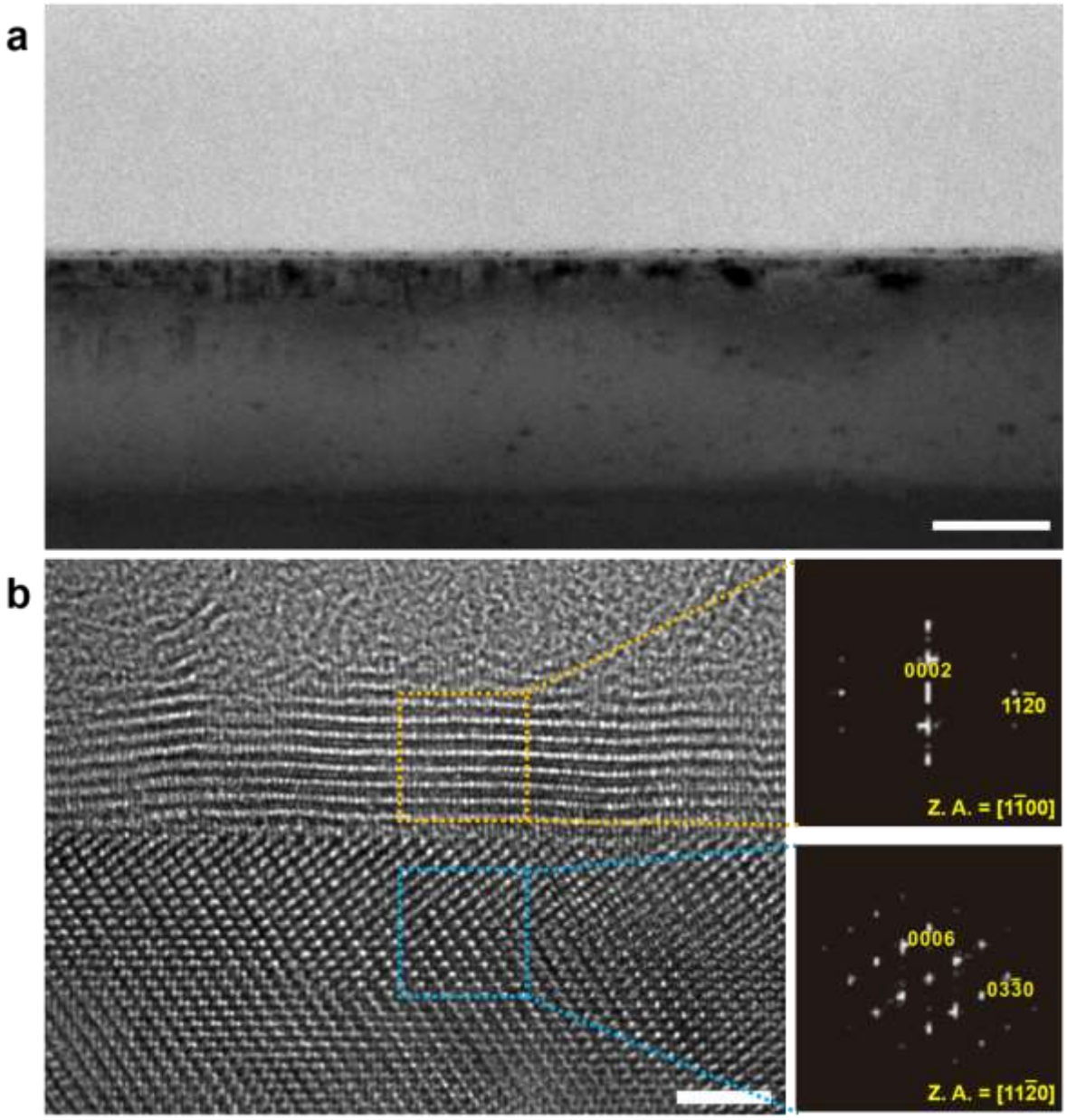

Figure S6. (**a**) Low-magnification TEM image of *EM*-h-BN on sapphire substrate. Scale bar is 50 nm. (**b**) Atomic resolution high-magnification TEM image and FFT patterns of *EM*-h-BN on sapphire substrate. Scale bar is 2 nm.

Figure S7. LEED pattern of bare sapphire substrate at 95 eV.

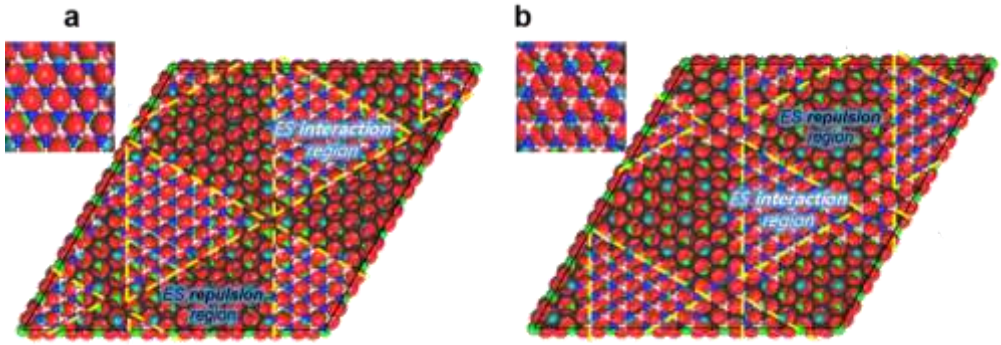

Figure S8. Base unit cells of (**a**) *R*30°, and (**b**) *R*90° configurations illustrated by Boron (salmon color) and nitrogen (blue color), which are located at 0.304 nm (i.e. in average height) from the α-Al_2O_3 surface. The rest of h-BN are colored in black. Ball-and-stick model was used for h-BN and CPK model was used for α-Al_2O_3, where Al on the surface is blue-green, Al in the second layer is green, and oxygen is red.

Table S1. Binding energy between h-BN and half Al-terminated Al_2O_3. Data of cell parameters, studied Moiré structures, binding, van der Waals (vdW), and electrostatic (*ES*) energies between h-BN and α-Al_2O_3(0001) with a vacuum of at least 70 Å (i.e. cell parameter c is 100 Å for all considered models). Superscript asterisk (*) respresents Moiré structures modeled by using based vectors of *R90*°.

Cell parameters		Rotation angle (θ)	Pair indies (n, m)	Binding energy (kcal/mol)	vdW energy (kcal/mol)	*ES* energy (kcal/mol)
a (Å)	*b* (Å)					
138.251	138.251	2.204	(3, 1)*	-1.56907	-1.53977	-0.02930
101.449	101.449	8.213	(1, 2)	-1.56900	-1.53987	-0.02912
167.138	167.138	16.826	(2, 3)	-1.56960	-1.54011	-0.02949
38.344	38.344	30	(1, 1)	-1.57735	-1.54036	-0.03699
167.138	167.138	43.174	(3, 2)	-1.56944	-1.54000	-0.02944
101.449	101.449	51.787	(2, 1)	-1.56874	-1.53971	-0.02904
138.251	138.251	57.796	(1, 3)*	-1.56875	-1.53958	-0.02916
138.251	138.251	62.204	(3, 1)	-1.56870	-1.53956	-0.02914
101.449	101.449	68.213	(1, 2)*	-1.56852	-1.53959	-0.02893
167.138	167.138	76.826	(2, 3)*	-1.56833	-1.53946	-0.02887
38.344	38.344	90	(1, 1)*	-1.56964	-1.53759	-0.03205
167.138	167.138	103.174	(3, 2)*	-1.56850	-1.53957	-0.02893
101.449	101.449	111.787	(2, 1)*	-1.56878	-1.53976	-0.02902
138.251	138.251	117.796	(1, 3)	-1.56903	-1.53975	-0.02928

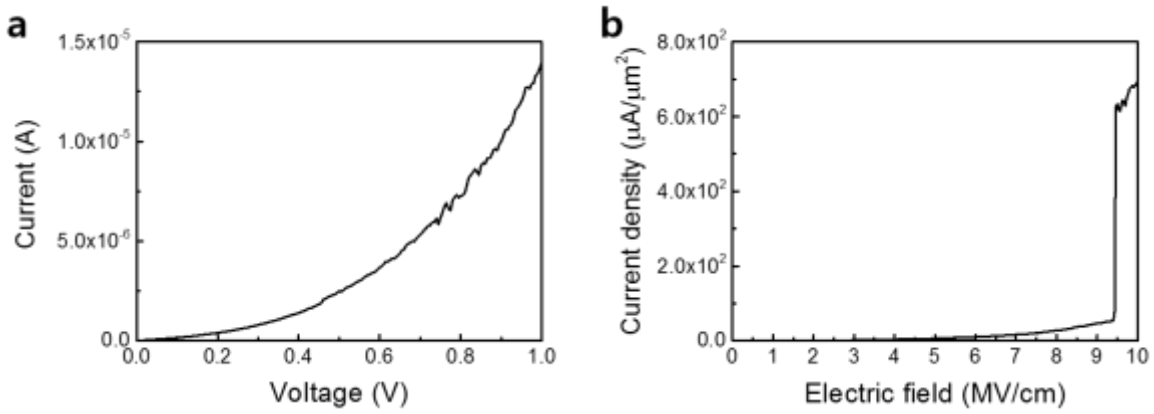

Figure S9. Characteristic I-V curves for Au/*EM*-h-BN/Au device. Representative (a) tunneling current and (b) breakdown voltage measurement in the transferred *EM*-h-BN.

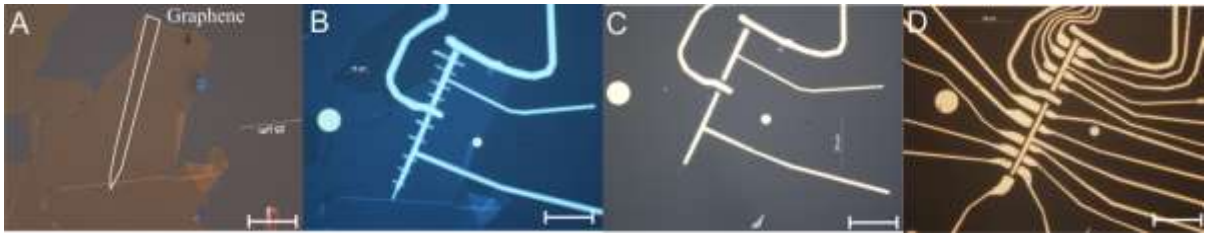

Figure S10. Schematic of the fabrication process for devices encapsulated with micro mechanically exfoliated h-BN (MME-h-BN) (**a**) mechanically exfoliated h-BN crystal used to lift exfoliated graphene from SiO_2 substrate. (**b**) The Al_2O_3 / *EM*-h-BN / MME graphene / MME-h-BN stack with added Au gate electrodes (50 nm) and Aluminum etch mask. (**c**) the structure after etching away MME-h-BN in a Freon plasma. (**d**) 1D contacts added to the MME-graphene encapsulated between *EM*-h-BN and MME-h-BN (Scale bar = 20 μm).

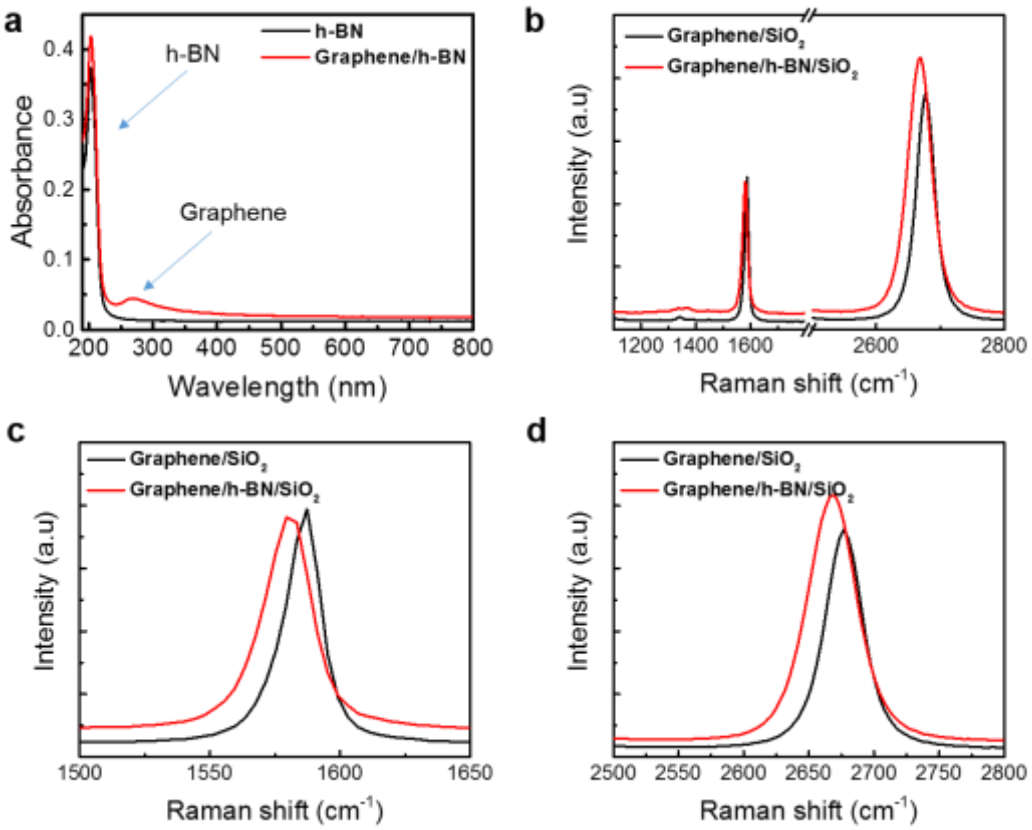

Figure S11. (**a**) UV-visible absorption and (**b**) Full range Raman spectrum of graphene on various substrates. (**c**) G peak, and (**d**) 2D peak position Raman spectra of graphene on various substrates.

References

1. Novoselov, K. S.; Jiang, D.; Schedin, F.; Booth, T. J.; Khotkevich, V. V.; Morozov, S. V.; Geim, A. K. *Proc. Natl. Acad. Sci. U.S.A.* **2005,** *102*, 10451-3.
2. Britnell, L.; Gorbachev, R. V.; Jalil, R.; Belle, B. D.; Schedin, F.; Katsnelson, M. I.; Eaves, L.; Morozov, S. V.; Mayorov, A. S.; Peres, N. M. R., et al. *Nano Lett.* **2012,** *12*, 1707-1710.
3. Kretinin, A. V.; Cao, Y.; Tu, J. S.; Yu, G. L.; Jalil, R.; Novoselov, K. S.; Haigh, S. J.; Gholinia, A.; Mishchenko, A.; Lozada, M., et al. *Nano Lett* **2014,** *14*, 3270-3276.
4. Wang, L.; Meric, I.; Huang, P. Y.; Gao, Q.; Gao, Y.; Tran, H.; Taniguchi, T.; Watanabe, K.; Campos, L. M.; Muller, D. A., et al. *Science* **2013,** *342*, 614-617.
5. Berciaud, S.; Ryu, S.; Brus, L. E.; Heinz, T. F. *Nano Lett.* **2009,** *9*, 346-352.
6. Wang, X.-G.; Chaka, A.; Scheffler, M. *Phys. Rev. Lett.* **2000,** *84*, 3650-3653.
7. Delley, B. *J. Chem. Phys.* **1990,** *92*, 508-517.
8. Delley, B. *J. Chem. Phys.* **2000,** *113*, 7756-7764.
9. Perdew, J. P.; Burke, K.; Ernzerhof, M. *Phys. Rev. Lett.* **1996,** *77*, 3865-3868.
10. Grimme, S. *J. Comput. Chem.* **2006,** *27*, 1787-1799.
11. Zhao, L.; Liu, L.; Sun, H. *J. PHys. Chem. C* **2007,** *111*, 10610-10617.
12. Saha, S.; Gadagkar, V.; Maiti, P. K.; Muthu, D. V. S.; Golberg, D.; Tang, C.; Zhi, C.; Bando, Y.; Sood, A. K. *J. Nanoscie. Nanotechnol.* **2007,** *7*, 1810-1814.
13. MUNRO, M. *J. Am. Ceram. Soc.* **1997,** *80*, 1919-1928.
14. Ji, C.; Levitas, V. I.; Zhu, H.; Chaudhuri, J.; Marathe, A.; Ma, Y. *Proc. Natl. Acad. Sci. U.S.A.* **2012,** *109*, 19108-19112.
15. Trambly de Laissardière, G.; Mayou, D.; Magaud, L. *Nano Lett.* **2010,** *10*, 804-808.
16. Zhang, X.; Xu, Z.; Hui, L.; Xin, J.; Ding, F. *J. Phys. Chem. Lett.* **2012,** *3*, 2822-2827.